Cold-formed steel strength predictions for torsion

Yu Xia[1], Robert S. Glauz[2], Benjamin W. Schafer[3], Michael Seek[4], Hannah B. Blum[5]

Abstract

Locally slender open cross-section members are susceptible to significant twisting and high warping torsion stresses. Torsion considerations are complicated by whether it is derived as a first-order effect from loading or a second-order effect from instability. Previous direct torsion experiments on lipped channels have shown significant inelastic reserve in limited cases. The current design for combined bending and torsion interaction has some limitations, including only considering the first yield in torsion and ignoring the cross-section slenderness in torsion. A parametric study is conducted to predict the torsion capacity in locally slender cross-sections. Shell finite element models of lipped Cee and Zee section members are validated with existing experiments on combined bending and torsion. The validated models are utilized for a parametric study with applied torsion on a range of cross-sections, steel grades, and members lengths to cover the range of practically expected torsional slenderness. A set of bimoment parameters, including yield bimoment, buckling bimoment, and plastic bimoment, are calculated and the ultimate bimoment is determined by performing shell finite element collapse analyses. A simple uniform equation is adopted to predict the bimoment capacity and two bimoment strength curves under torsion only are proposed for local and distortional buckling controlled cases respectively.

1. Introduction

Cold-formed steel (CFS) is a common construction material in which steel sheets are shaped into structural members by the cold-working processes and are widely used in many structural and non-structural applications. Among different types of CFS shapes, the thin-walled open sections (e.g., Cee and Zee) are the most common for structural framing. The thin-walled geometries are beneficial to reducing the self-weight, hence lower transportation, material costs, and labor costs. However, due to the open thin-walled geometries, CFS sections have a low torsional stiffness and can be vulnerable to even a small amount of torsional load. Therefore, understanding the internal torsional forces for CFS members is important to correctly conduct the member and structure design (Glauz, 2020).

---

[1]PhD Candidate, University of Wisconsin-Madison, <yxia44@wisc.edu>

[2]President/Owner, RSG Software, Inc., <glauz@rsgsoftware.com>

[3]Professor, Johns Hopkins University, <schafer@jhu.edu>

[4]Associate Professor, Old Dominion University, <mseek@odu.edu>

[5]Assistant Professor, University of Wisconsin-Madison, <hannah.blum@wisc.edu>

A member subjected to torsional loads may develop both shear stresses and longitudinal stresses. For typical open cross sections, the most critical internal force is the bimoment (B) caused by the longitudinal stresses. However, limited literature shows the method to calculate the bimoment strength, while a few design standards provide indirect methods to consider the effect resulting from torsional stresses. Section H4 of AISI S100 (2020) states that for members under combined bending and torsion, the flexural strength should be reduced by a reduction factor R, which is given as Eq. 1:

$$R = \frac{f_{bending,max}}{f_{bending} + f_{torsion}} \tag{1}$$

where $f_{bending,max}$ is the bending stress at extreme fiber, $f_{bending}$ is the bending stress at location in cross-section where combined bending and torsion stress is maximum, and $f_{torsion}$ is the torsional warping stress at location in cross-section where combined bending and torsion stress is maximum.

Section 6.1.6 of Eurocode 3 Part 1-3 (European Committee for Standardization (CEN), 2006) stipulates the upper bound of the total longitudinal stress and the total shear stress for members under combined bending and torsion as shown in Eq. 2:

$$\sqrt{\sigma_{tot,Ed}^2 + 3\tau_{tot,Ed}^2} \leq 1.1\frac{f_{ya}}{\gamma_{MO}} \tag{2}$$

where $\sigma_{tot,Ed}$ is the design total direct stress, calculated on the relevant effective cross-section, $\tau_{tot,Ed}$ is the design total shear stress, calculated on the gross cross-section, f_{ya} is the steel average yield strength, and γ_{MO} is a safety factor.

Section 5.3.2 of GB 50018 (Ministry of Construction of the P.R.C and General Administration of Quality Supervision, Inspection and Quarantine of the P.R.C, 2002, Chinese version) stipulates the upper bound of the sum of normalized bending moment and bimoment as shown in Eq. 3, which is transformed into Eq. 4 by Wan et al. (2021):

$$\sigma = \frac{M}{W_{enx}} + \frac{B}{W_{\omega}} \leq f \tag{3}$$

$$\frac{M}{M_b} + \frac{B}{B_y} \leq 1 \tag{4}$$

where M_b is the bending capacity under bending moment only and B_y is the bimoment capacity under torsion only.

These standards consider the reduction for yield moment and bimoment, while member inelastic behaviors are not sufficiently considered.

Wan et al. (2021) carried out an experimental campaign to investigate the torsional strength of a pair of Cee and Zee sections under combined bending and torsion caused by vertical loads at different eccentricities. The experimental results were compared with Eq. 4 and the comparison showed the design equation is very conservative, particularly for Zee sections. Bian et al. (2016) investigated the member behavior of a set of Cee section short beams under torsion only by both experimental and numerical study. Based on the experimental results and the simulation results with expanded torsional slenderness and strengths, two groups of piecewise equations predicting the torsion capacity were provided as shown in Eq. 5 with parabolic inelastic reserve and Eq. 6 with linear inelastic reserve:

$$\frac{T_n}{T_y} = \begin{cases} 2 - \lambda_T^2 & \text{for } \lambda_T \leq 1 \\ 1/\lambda_T^2 & \text{for } \lambda_T > 1 \end{cases} \tag{5}$$

$$\frac{T_n}{T_y} = \begin{cases} 2.5 - 1.5\lambda_T & \text{for } \lambda_T \leq 1 \\ 1/\lambda_T^2 & \text{for } \lambda_T > 1 \end{cases} \tag{6}$$

where T_n is the torsional strength, T_y is the torque at first yield, $\lambda_T = \sqrt{T_y/T_{cr}}$ is the torsional slenderness, and T_{cr} is the critical elastic torsional buckling moment.

However, the data used in the numerical study only included one Cee section (400S162-54). Other Cee section geometries as well as Zee sections should also be investigated. Furthermore, it is desirable to determine if the torsional strength can be predicted by a simpler and uniform equation in lieu of piecewise equations.

In this paper, a numerical study is carried out to predict the bimoment capacity of thin-walled CFS Cee and Zee sections under torsional load. Firstly, a finite element model is developed and validated by the benchmark data reported previously (Wan, Huang, and Mahendran, 2021) which considered combined torsion and bending loading. Then the validated model is modified for applied torsional loads only and the model is used in a parametric study. Various Cee and Zee sections from design manuals, various steel grades, and various member lengths were investigated. Bimoment parameters, including yield bimoment, buckling bimoment, and plastic bimoment, are calculated based on the member cross section geometry and yield strength. The ultimate bimoment for each case is also calculated from the longitudinal stresses obtained from finite element analyses. Based on the relationship between the ultimate bimoment and other bimoment parameters, a single continuous equation with only two numerical coefficients is adopted for the bimoment strength calculation. In addition, for local buckling (LB) and distortional buckling (DB) controlled cases, two groups of equation coefficients are provided.

2. Development and validation of torsion finite element model

A finite element model was designed and developed based on a combined torsion and bending experimental study (Wan, Huang, and Mahendran, 2021). Firstly, to guarantee the reliability of the model, the model was developed to simulate the experiment from all aspects and the simulation results were compared directly with the experiment results. Then, upon completion of model
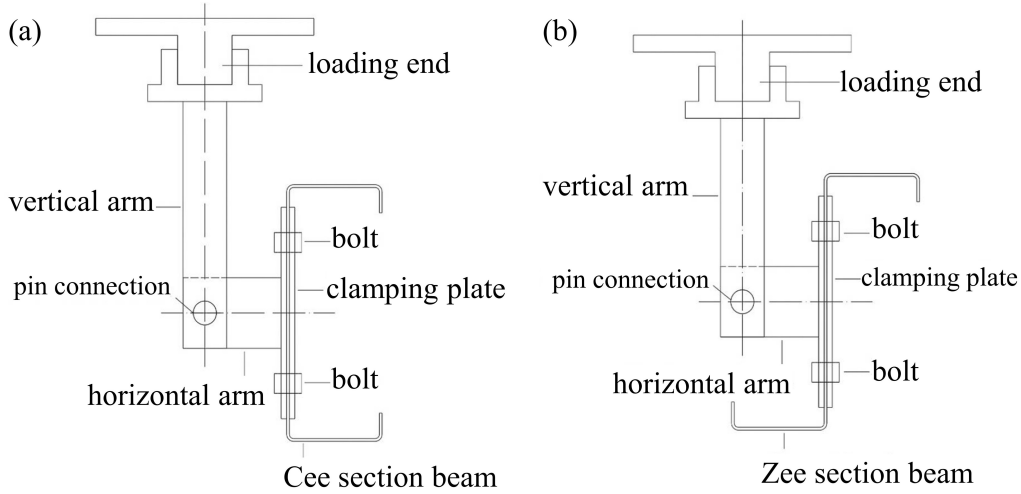
Figure 1: Loading method for (a) Cee section beam and (b) Zee section beam (Fig. 5 from Wan, Huang, and Mahendran, 2021)

validation, the model was adjusted to support a parametric study of members under torsion only by adopting different cross section geometries and different material definitions.

The experimental study (Wan, Huang, and Mahendran, 2021) investigated the member behaviors of press-braked CFS Cee and Zee sections under combined bending and torsion. The study included two cross section geometries ($180 \times 70 \times 20 \times 2.5$ and $185 \times 70 \times 20 \times 1.8$ in the form of $D \times B \times d \times t$ in mm, where D, B, and d are the outer-to-outer web depth, flange width, and lip length, t is the thickness) for Cee and Zee respectively, where the yield strength for the 2.5 mm thick steel is 345 MPa and for the 1.8 mm thick steel is 318 MPa. For each cross section geometry, two different member lengths (1200 mm and 1500 mm) were included. The members were simply-supported and loaded under an eccentric vertical load at mid-span, where the vertical load introduced the bending and the eccentricity of the load introduced the torsion. For each case, three different eccentricities on the side away from the top flange (30, 40, and 50 for Cee, and 40, 50, and 60 for Zee, in mm) were investigated. A schematic diagram from the literature (Wan, Huang, and Mahendran, 2021) is shown in Fig. 1 to help readers better visualize the test setup.

The finite element model was developed using FEA software Abaqus (Abaqus, 2016). The member was modeled by S4R shell elements, and each element had an aspect ratio between 0.5 and 2 except those at the corners. The material was modeled as elastic-perfectly-plastic (EPP) using the yield strengths from the experiments and $E = 203$ GPa recommended by AISI S100 (2020). By adopting the principle of force transmissibility as illustrated in Fig. 2, the eccentric vertical load was transformed into a vertical load P directly acting on the juncture of web and top flange and a pair of lateral loads Q with opposite directions acting on the juncture of web and top flange as well as the juncture of web and bottom flange respectively. Different eccentricities reflected the relationship between P and $Q = P(ds + e)/D$, where ds is the horizontal distance between the web center and shear center. For the boundary conditions at the two Cee or Zee ends, the nodes were restrained in the cross section plane, thus the rotation about the member longitudinal direction was automatically restrained. The nodes at two ends were free to move in the longitudinal direction
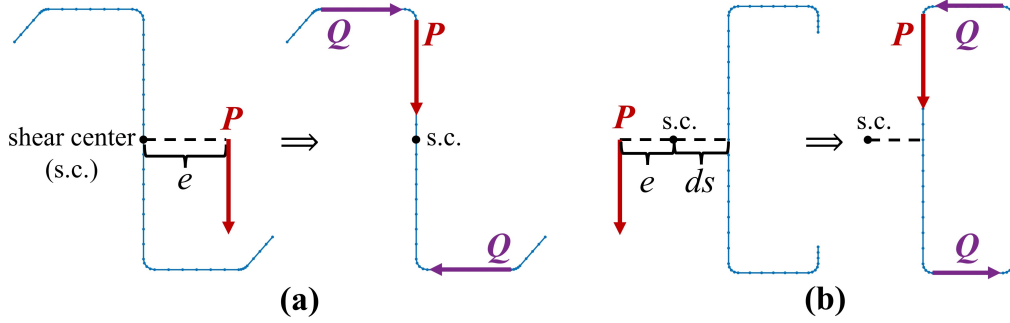
4

Figure 2: Transformation of eccentrically load for (a) Zee section and (b) Cee section
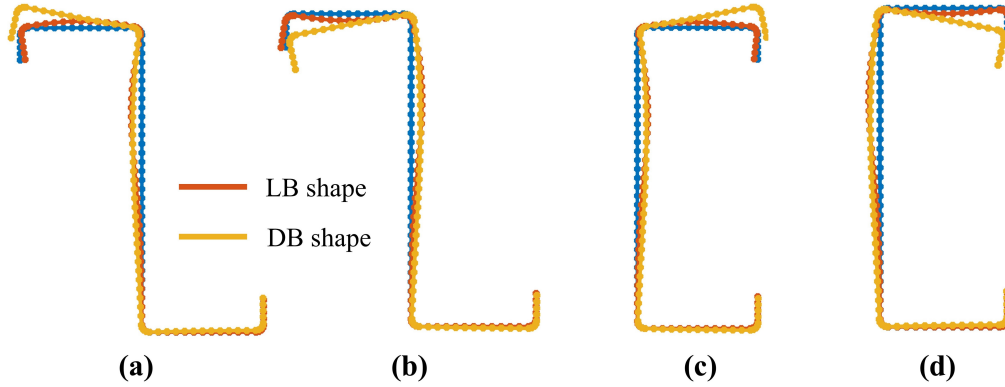

Figure 3: Typical buckled shapes under bending generated in CUFSM (Li and Schafer, 2010) as initial GI for (a) Zee section outward shape, (b) Zee section inward shape, (c) Cee section outward shape, and (d) Cee section inward shape

based on a longitudinal warping free assumption. At midspan, all nodes along one cross section were restrained in the longitudinal direction to prevent rigid body motion. Both scenarios without and with initial geometric imperfection (GI) were studied. The buckled shapes corresponding to the local and distortional minima of signature curves due to bending generated in CUFSM's (Li and Schafer, 2010) finite strip analyses were selected as the shapes of initial GI. Both inward and outward GI shapes were considered, where *inward* and *outward* describe the deformation direction of top flange for local buckling (LB) and lip-flange juncture for distortional buckling (DB) as illustrated in Fig. 3. Either the inward or outward GI shape was generated from CUFSM analyses, and the other GI shape was determined by switching the sign of the displaced nodes (ΔY and ΔZ as shown in Fig 8) of the cross-section. The average magnitudes of GI summarized in Zeinoddini-Meimand, 2011 ($0.47t$ for LB and $1.03t$ for DB) were selected as as the maximum magnitudes of the GI shapes. The residual stress was not included. The simulations were conducted using Abaqus' Riks solver to obtain a post-peak response.

The magnitude of the peak applied vertical load P was extracted from the simulations as the major result. The comparison of peak P between the experiment (Wan, Huang, and Mahendran, 2021) and the simulations is shown in Fig. 4. There are two results with geometric imperfections for each case – one considering inward imperfections (Fig. 3(b) and (d)) and the other considering outward imperfections (Fig. 3(a) and (c)). For most cases, the experimental data is between the corresponding simulation data with and without GI. The average ratio between the experimental
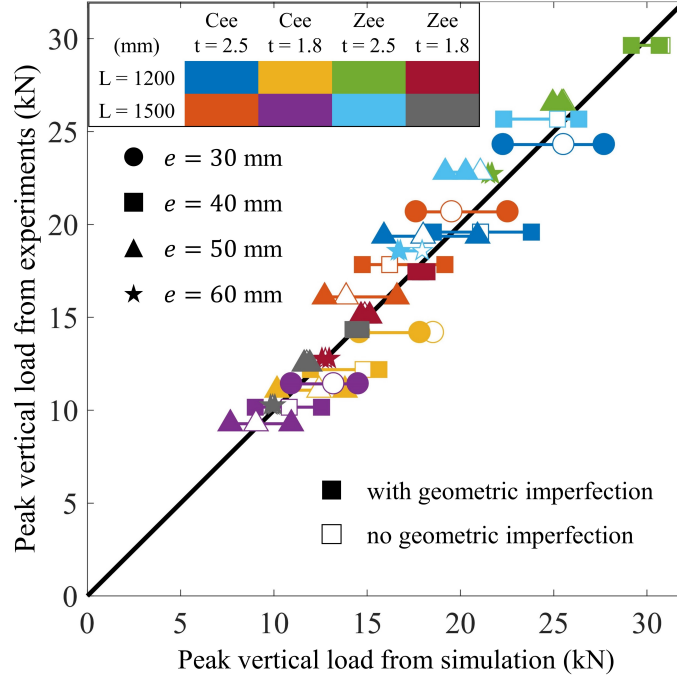
Figure 4: Comparison between the results of the experimental study (Wan, Huang, and Mahendran, 2021) and the developed Abaqus model

peak P and the peak P from simulation without GI is 99.4%. The average ratio between the experimental peak P and the average peak P from simulation with GI is 101.7%. The average ratio between the experimental peak P and the average peak P from all simulations with and without GI is 100.8%. The excellent agreement indicates the experimental setup can be well represented by the developed finite element model.

3.   Data from simulation for parametric study

The validated FEA model was adjusted to accommodate the scenario under torsional loads only for the thin-walled CFS members. Firstly, the vertical load P introducing bending was removed. The couple created by lateral forces Q was used to represent applied torsional loads and vertical load P was removed from the model. In addition, to develop a case with bimoment only at midspan, the applied load was transformed from concentrated torsion to uniformly distributed torsion along member longitudinal direction, where the magnitude of the uniformly distributed torsion $q = Q/L$ and L is the member length.

Secondly, steel with various grades and stress-strain behaviors was included. The primary cases included mild steel (Mild-1x) with a yield strength of 50 ksi (345 MPa) for Cee (Steel Stud Manufacturers Association (SSMA), 2015) and 55 ksi (379 MPa) for Zee (American Iron and Steel Institute (AISI), 2017) and the stress-strain behavior of the mild steel was described by the EPP model. In addition, higher steel grades were included to investigate the cases with higher torsional slenderness. A few cases of mild steel with doubled (Mild-2x) and quadruple (Mild-4x) yield strength were modeled using the EPP model. The elastic moduli for all mild steel were 203 GPa. In addition, a few supplementary cases using Martensitic steel (MS-1200) with a nominal yield
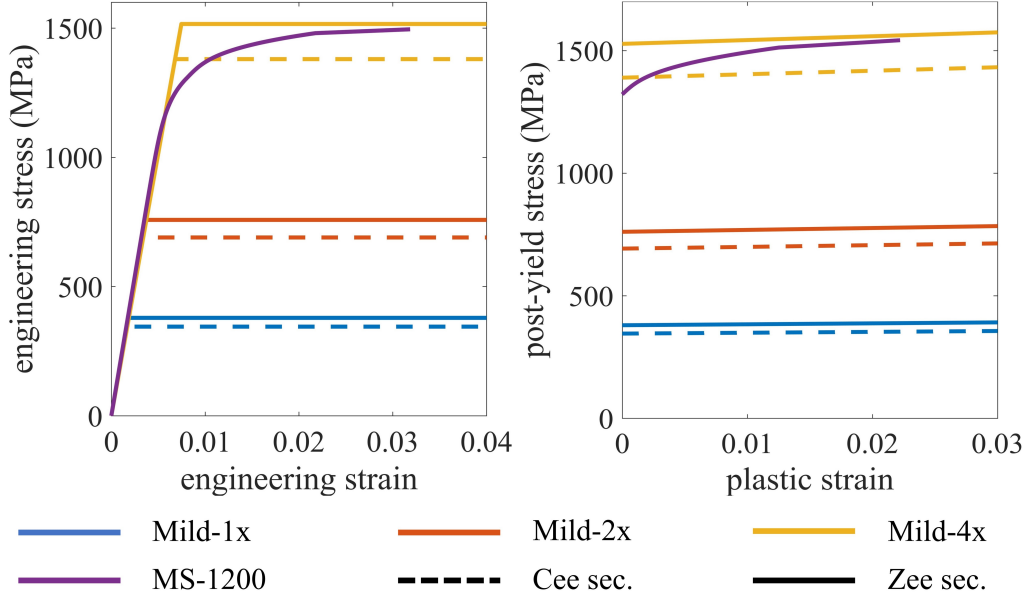
Figure 5: Constitutive relationships for steel adopted in finite element models

strength of 1200 MPa were included, which showed a rounded stress-strain relationship and was modeled by the two-stage plus linear model (Xia et al., 2021). The average of the tensile coupon test experimental data was adopted for MS-1200, where the elastic modulus was 215,684 MPa (Xia et al., 2021) and the yield strength ($\sigma_{0.2}$) was 1307 MPa. The material definition of MS-1200 for Zee and Cee cross sections were identical. The engineering stress-strain relationship and the relationship between plastic strain and post-yield stress for each steel are shown in Fig. 5.

Thirdly, the member geometry was expanded and the initial imperfections were adjusted. Typical cross section sizes from AISI D100 (2017) and SSMA product technical guide (2015) were selected as shown in Table 1. The initial GI shapes for local and distortional buckling were determined through a finite strip analysis in CUFSM (Li and Schafer, 2010) where the member was subjected to bimoment only. The applicable local and distortional minima provided the buckled shapes. Zee sections under counterclockwise torsion (web in compression) only have a local buckling minimum, therefore only the local buckling shape was adopted as the initial GI shape for this case. A typical example of initial imperfection shapes for torsion are shown in Figure 6. The maximum magnitudes of the imperfections are the same as discussed in Section 2. ($0.47t$ for LB and $1.03t$ for DB). The member length (L) was also adjusted so that it was dependent on the web depth D of cross section. For Mild-1x, Mild-4x, and MS-1200, $L = 10D$. In addition, a few cases with shorter span lengths were investigated to compare the effect of different spans on member behavior, which included $L = 6D$ for Mild-2x and $L = 3D$ for Mild-4x. Also, to compare the influence of the lip length on buckling behavior, a group of Cee sections, with $10D$ member length and Mild-1x material, had the lip length increased from 0.625 inch (15.875 mm) to 1.0 inch (25.4 mm).

For each cross section, simulation for both torsion directions, clockwise (CW) and counterclockwise (CCW) about the member longitudinal axis, were run for Mild-1x with $L = 10D$, and the

7

Table 1: Selected cross sections for the parametric study

Cee cross section			
1200S300x97	1000S300x97	800S250x97	600S200x97
1200S300x68	1000S300x68	800S250x68	600S200x68
1200S300x54	1000S300x54	800S250x54	600S200x54
Zee cross section			
12Z325x105	10Z325x105	8Z275x105	6Z225x105
12Z325x070	10Z325x070	8Z275x070	6Z225x070
12Z325x059	10Z325x059	8Z275x059	6Z225x059

(a)   (b)   (c)   (d)

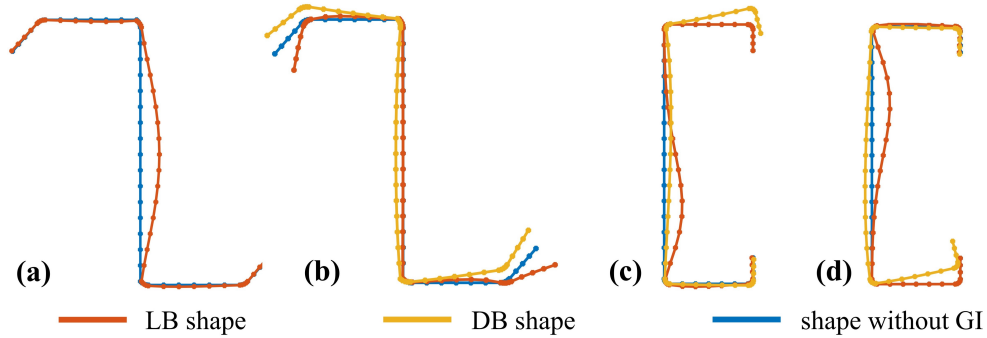——— LB shape   ——— DB shape   ——— shape without GI

Figure 6: Typical buckled shapes generated in CUFSM (Li and Schafer, 2010) as initial GI for (a) Zee section under counterclockwise torsion, (b) Zee section under clockwise torsion, (c) Cee section under counterclockwise torsion, and (d) Cee section under clockwise torsion

internal bimoment B at midspan was calculated by using the nodal longitudinal stresses at midspan when peak q was achieved. The results showed that the bimoments of Zee sections for the opposite torsion cases were substantially different, while the bimoments for Cee sections under the opposite torsions were almost the same in magnitude (within 0.3% difference). Therefore, for the other steel grades, member lengths, or lip lengths, cases of both directions of torsions were investigated for Zee sections, while only one direction of torsion was studied for Cee sections, as illustrated in Fig. 7. In addition, from the initial simulations, the difference of the internal bimoment B calculated at midspan between cases with and without GI was minor, where the average difference was within 1%. Therefore, only the cases with GI were investigated for the parametric study to mimic the more realistic scenario.
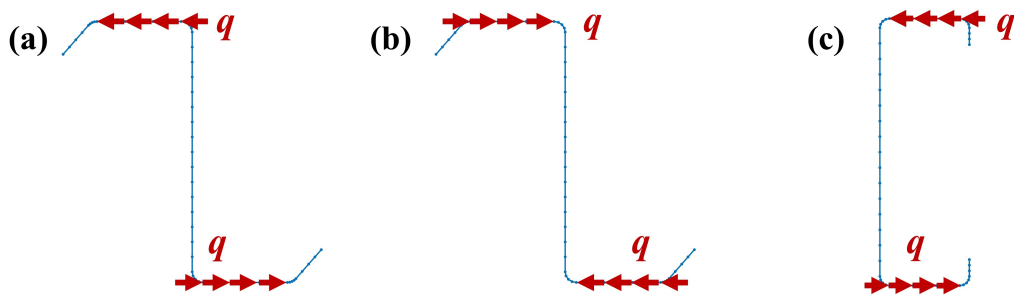

(a) q (b) q (c) q
       q q q

Figure 7: Torsion loading cases: (a) CCW torsion for Zee section; (b) CW torsion for Zee section; (c) CCW torsion for Cee section
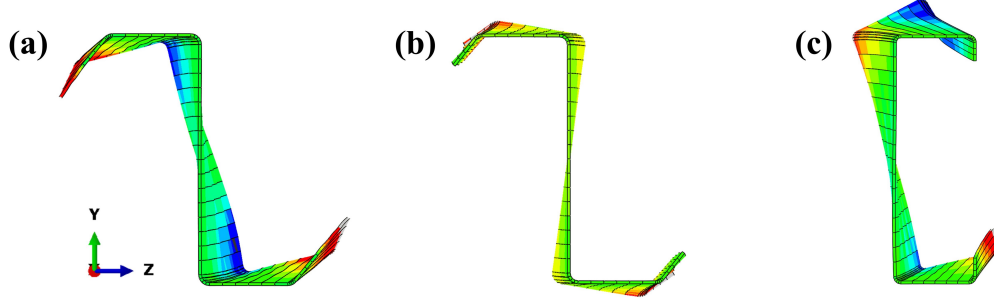
8

Figure 8: Examples (6Z225x070, Mild-1x-10D for (a) and (b), and 600S200x68, Mild-1x-10D for (c)) of the side view (YZ plane) of the deformed shapes (scale factor=1) at peak applied torsion for (a) CCW torsion case showing LB behavior, (b) CW torsion case showing DB behavior, and (c) CCW torsion case showing DB behavior

By comparing the deformed shapes at peak applied torsion with the local and distortional deformed shapes under torsion generated by CUFSM (Li and Schafer, 2010), each case was categorized as local buckling (LB) or distortional buckling (DB) controlled case. The results and the post-processed data of the simulation are shown in Table 2 for LB controlled cases and Table 3 for DB controlled cases. Fig. 8 shows typical examples of side view (YZ plane) of the deformed shapes at peak applied load under CCW and CW torsion. The steel grade, member length, and loading direction were combined and given as *Type* in Table 2 and 3. For example, Mild-1x-10D-CCW for section 1200S300x97 represents the case for a member 1200S300x97 under CCW torsion (Fig. 7), where the member is made of Mild-1x and member length is $10D$. The only exception is type LargeLip-10D-CCW, where the member for this type is made of Mild-1x and its lip length is 1 inch.

Furthermore, the yield bimoment B_y, the plastic bimoment B_p, and the buckling bimoment B_{cr} are given for each case. B_y and B_p are calculated based on the yield strength and cross section geometry. B_{cr} is calculated by CUFSM (Li and Schafer, 2010). In addition, by using Eq. 7, the internal ultimate bimoment $B_{n\sigma}$ for each case at midspan is calculated by the longitudinal nodal stresses when the peak applied distributed torsion $m_t = q \times D$ is achieved:

$$
B_{n\sigma} = \int \sigma w_n dA = \sum_{i=1}^{N-1} t_i l_i \sigma_i \left(w_{ni} + \frac{1}{2} R_{oi} l_i \right) + \frac{1}{2} t_i l_i (\sigma_{i+1} - \sigma_i) \left(w_{ni} + \frac{2}{3} R_{oi} l_i \right) \qquad (7)
$$

where element i is defined from node i to node $i+1$, N is the number of nodes on the cross section, l_i is the length of element i, t_i is the thickness of element i, σ_i is the longitudinal stress at node i, w_{ni} is the normalized unit warping at node i, R_{oi} is perpendicular distance between the shear center and element i.

The results show the calculated internal bimoment $B_{n\sigma}$ is larger than B_y and B_{crl} for most LB controlled cases, while $B_{n\sigma}$ is between B_y and B_{crd} for most DB controlled cases. Also, $B_{n\sigma}$ is smaller than B_p for almost all cases.

Table 2: Results for cases showing controlling LB behaviors

Section	Type	B_p kN-m^2	B_y kN-m^2	B_{crl} kN-m^2	$B_{n\sigma}$ kN-m^2	λ_B	B_{npred} kN-m^2	$\frac{B_{n\sigma}}{B_p}$	$\frac{B_{n\sigma}}{B_{npred}}$
12Z325x105	Mild-1x-10D-CCW	1.681	0.878	0.751	1.564	1.08	1.471	0.93	1.06
12Z325x070	Mild-1x-10D-CCW	1.110	0.580	0.222	0.879	1.62	0.864	0.79	1.02
12Z325x059	Mild-1x-10D-CCW	0.932	0.488	0.133	0.703	1.91	0.681	0.75	1.03
10Z325x105	Mild-1x-10D-CCW	1.404	0.778	0.850	1.302	0.96	1.260	0.93	1.03
10Z325x070	Mild-1x-10D-CCW	0.928	0.514	0.251	0.729	1.43	0.752	0.79	0.97
10Z325x059	Mild-1x-10D-CCW	0.779	0.432	0.150	0.588	1.70	0.596	0.76	0.99
8Z275x105	Mild-1x-10D-CCW	0.868	0.472	0.764	0.814	0.79	0.804	0.94	1.01
8Z275x070	Mild-1x-10D-CCW	0.573	0.312	0.225	0.488	1.18	0.491	0.85	0.99
8Z275x059	Mild-1x-10D-CCW	0.481	0.262	0.135	0.375	1.40	0.393	0.78	0.95
6Z225x105	Mild-1x-10D-CCW	0.482	0.257	0.688	0.487	0.61	0.460	1.01	1.06
6Z225x070	Mild-1x-10D-CCW	0.318	0.170	0.202	0.283	0.92	0.288	0.89	0.98
6Z225x059	Mild-1x-10D-CCW	0.267	0.142	0.121	0.225	1.09	0.234	0.84	0.96
12Z325x105	Mild-4x-10D-CCW	6.725	3.511	0.751	4.663	2.16	4.667	0.69	1.00
12Z325x070	Mild-4x-10D-CCW	4.442	2.321	0.222	2.660	3.23	2.590	0.60	1.03
12Z325x105	MS-1200-10D-CCW	6.725	3.511	0.751	4.548	2.16	4.667	0.68	0.97
6Z225x059	MS-1200-10D-CCW	1.070	0.569	0.121	0.635	2.17	0.741	0.59	0.86
12Z325x105	Mild-2x-6D-CCW	3.362	1.756	0.751	2.839	1.53	2.668	0.84	1.06
12Z325x070	Mild-2x-6D-CCW	2.221	1.161	0.222	1.593	2.28	1.505	0.72	1.06
12Z325x059	Mild-2x-6D-CCW	1.865	0.975	0.133	1.226	2.71	1.174	0.66	1.04
10Z325x105	Mild-2x-6D-CCW	2.808	1.555	0.850	2.353	1.35	2.317	0.84	1.02
10Z325x070	Mild-2x-6D-CCW	1.855	1.029	0.251	1.331	2.03	1.323	0.72	1.01
10Z325x059	Mild-2x-6D-CCW	1.558	0.865	0.150	1.029	2.40	1.034	0.66	1.00
8Z275x105	Mild-2x-6D-CCW	1.736	0.945	0.764	1.496	1.11	1.509	0.86	0.99
8Z275x070	Mild-2x-6D-CCW	1.146	0.624	0.225	0.862	1.67	0.882	0.75	0.98
8Z275x059	Mild-2x-6D-CCW	0.962	0.524	0.135	0.674	1.97	0.694	0.70	0.97
6Z225x105	Mild-2x-6D-CCW	0.965	0.514	0.688	0.866	0.86	0.881	0.90	0.98
6Z225x070	Mild-2x-6D-CCW	0.637	0.339	0.202	0.506	1.29	0.532	0.79	0.95
6Z225x059	Mild-2x-6D-CCW	0.535	0.285	0.121	0.402	1.54	0.424	0.75	0.95
12Z325x070	Mild-4x-3D-CCW	4.442	2.321	0.222	2.696	3.23	2.590	0.61	1.04
12Z325x059	Mild-4x-3D-CCW	3.730	1.950	0.133	2.009	3.83	2.031	0.54	0.99
10Z325x070	Mild-4x-3D-CCW	3.710	2.058	0.251	2.260	2.86	2.278	0.61	0.99
10Z325x059	Mild-4x-3D-CCW	3.116	1.729	0.150	1.687	3.40	1.780	0.54	0.95
8Z275x105	Mild-4x-3D-CCW	3.473	1.889	0.764	2.732	1.57	2.729	0.79	1.00
8Z275x070	Mild-4x-3D-CCW	2.292	1.249	0.225	1.514	2.36	1.532	0.66	0.99
8Z275x059	Mild-4x-3D-CCW	1.924	1.049	0.135	1.147	2.79	1.195	0.60	0.96
6Z225x105	Mild-4x-3D-CCW	1.930	1.027	0.688	1.562	1.22	1.639	0.81	0.95
6Z225x070	Mild-4x-3D-CCW	1.274	0.678	0.202	0.916	1.83	0.946	0.72	0.97
6Z225x059	Mild-4x-3D-CCW	1.070	0.569	0.121	0.700	2.17	0.741	0.65	0.94

Table 3: Results for cases showing controlling DB behaviors

Section	Type	B_p kN-m^2	B_y kN-m^2	B_{crd} kN-m^2	$B_{n\sigma}$ kN-m^2	λ_B	B_{npred} kN-m^2	$\frac{B_{n\sigma}}{B_p}$	$\frac{B_{n\sigma}}{B_{npred}}$
1200S300x97	Mild1x-10D-CCW	0.975	0.523	1.113	0.645	0.69	0.641	0.66	1.01
1200S300x68	Mild1x-10D-CCW	0.713	0.384	0.523	0.386	0.86	0.393	0.54	0.98
1200S300x54	Mild1x-10D-CCW	0.578	0.312	0.321	0.282	0.99	0.278	0.49	1.02
1000S300x97	Mild1x-10D-CCW	0.788	0.412	0.919	0.600	0.67	0.526	0.76	1.14
1000S300x68	Mild1x-10D-CCW	0.577	0.303	0.433	0.327	0.84	0.325	0.57	1.01
1000S300x54	Mild1x-10D-CCW	0.467	0.246	0.268	0.216	0.96	0.231	0.46	0.93

Table 3 continued from previous page

Section	Type	B_p kN-m^2	B_y kN-m^2	B_{crd} kN-m^2	$B_{n\sigma}$ kN-m^2	λ_B	B_{npred} kN-m^2	$\frac{B_{n\sigma}}{B_p}$	$\frac{B_{n\sigma}}{B_{npred}}$
800S250x97	Mild1x-10D-CCW	0.449	0.234	0.764	0.342	0.55	0.335	0.76	1.02
800S250x68	Mild1x-10D-CCW	0.331	0.174	0.363	0.232	0.69	0.216	0.70	1.07
800S250x54	Mild1x-10D-CCW	0.269	0.141	0.225	0.150	0.79	0.158	0.56	0.94
600S200x97	Mild1x-10D-CCW	0.223	0.116	0.600	0.222	0.44	0.183	1.00	1.21
600S200x68	Mild1x-10D-CCW	0.166	0.087	0.287	0.140	0.55	0.125	0.84	1.13
600S200x54	Mild1x-10D-CCW	0.136	0.071	0.179	0.095	0.63	0.094	0.70	1.01
12Z325x105	Mild1x-10D-CW	1.681	0.878	1.334	1.081	0.81	0.972	0.64	1.11
12Z325x059	Mild1x-10D-CW	0.932	0.488	0.361	0.448	1.16	0.373	0.48	1.20
10Z325x105	Mild1x-10D-CW	1.404	0.778	1.190	0.896	0.81	0.814	0.64	1.10
10Z325x070	Mild1x-10D-CW	0.928	0.514	0.473	0.489	1.04	0.420	0.53	1.16
10Z325x059	Mild1x-10D-CW	0.779	0.432	0.320	0.362	1.16	0.312	0.46	1.16
8Z275x105	Mild1x-10D-CW	0.868	0.472	0.945	0.555	0.71	0.558	0.64	0.99
8Z275x070	Mild1x-10D-CW	0.573	0.312	0.375	0.321	0.91	0.298	0.56	1.08
8Z275x059	Mild1x-10D-CW	0.481	0.262	0.254	0.241	1.02	0.224	0.50	1.07
6Z225x105	Mild1x-10D-CW	0.482	0.257	0.686	0.335	0.61	0.341	0.69	0.98
6Z225x070	Mild1x-10D-CW	0.318	0.170	0.275	0.192	0.79	0.189	0.60	1.02
6Z225x059	Mild1x-10D-CW	0.267	0.142	0.188	0.145	0.87	0.145	0.54	1.00
1200S300x97	Mild1x-10D-CW	0.975	0.523	1.113	0.645	0.69	0.641	0.66	1.01
1200S300x68	Mild1x-10D-CW	0.713	0.384	0.523	0.386	0.86	0.393	0.54	0.98
1200S300x54	Mild1x-10D-CW	0.578	0.312	0.321	0.282	0.99	0.278	0.49	1.01
1000S300x97	Mild1x-10D-CW	0.788	0.412	0.919	0.600	0.67	0.526	0.76	1.14
1000S300x68	Mild1x-10D-CW	0.577	0.303	0.433	0.327	0.84	0.325	0.57	1.01
1000S300x54	Mild1x-10D-CW	0.467	0.246	0.268	0.217	0.96	0.231	0.46	0.94
800S250x97	Mild1x-10D-CW	0.449	0.234	0.764	0.341	0.55	0.335	0.76	1.02
800S250x68	Mild1x-10D-CW	0.331	0.174	0.363	0.232	0.69	0.216	0.70	1.07
800S250x54	Mild1x-10D-CW	0.269	0.141	0.225	0.150	0.79	0.158	0.56	0.94
600S200x97	Mild1x-10D-CW	0.223	0.116	0.600	0.222	0.44	0.183	1.00	1.21
600S200x68	Mild1x-10D-CW	0.166	0.087	0.287	0.140	0.55	0.125	0.84	1.13
600S200x54	Mild1x-10D-CW	0.136	0.071	0.179	0.095	0.63	0.094	0.70	1.01
1200S300x97	Mild4x-10D-CCW	3.899	2.091	1.113	1.168	1.37	1.264	0.30	0.92
1200S300x68	Mild4x-10D-CCW	2.853	1.537	0.523	0.569	1.71	0.669	0.20	0.85
1200S300x54	Mild4x-10D-CCW	2.311	1.248	0.321	0.462	1.97	0.435	0.20	1.06
1000S300x68	Mild4x-10D-CCW	2.306	1.212	0.433	0.558	1.67	0.562	0.24	0.99
1000S300x54	Mild4x-10D-CCW	1.868	0.984	0.268	0.370	1.92	0.368	0.20	1.01
800S250x68	Mild4x-10D-CCW	1.324	0.695	0.363	0.423	1.38	0.424	0.32	1.00
800S250x54	Mild4x-10D-CCW	1.076	0.566	0.225	0.278	1.59	0.284	0.26	0.98
600S200x97	Mild4x-10D-CCW	0.891	0.464	0.600	0.482	0.88	0.480	0.54	1.01
600S200x68	Mild4x-10D-CCW	0.665	0.347	0.287	0.274	1.10	0.284	0.41	0.96
600S200x54	Mild4x-10D-CCW	0.544	0.284	0.179	0.187	1.26	0.197	0.34	0.95
12Z325x070	Mild4x-10D-CW	4.442	2.321	0.528	0.706	2.10	0.756	0.16	0.93
12Z325x059	Mild4x-10D-CW	3.730	1.950	0.361	0.484	2.32	0.533	0.13	0.91
6Z225x059	Mild4x-10D-CW	1.070	0.569	0.188	0.214	1.74	0.245	0.20	0.87
1200S300x97	MS1200-10D-CCW	3.899	2.091	1.113	1.276	1.37	1.264	0.33	1.01
1200S300x54	MS1200-10D-CCW	2.311	1.248	0.321	0.477	1.97	0.435	0.21	1.10
1000S300x68	MS1200-10D-CCW	2.306	1.212	0.433	0.582	1.67	0.562	0.25	1.04
1000S300x54	MS1200-10D-CCW	1.868	0.984	0.268	0.389	1.92	0.368	0.21	1.06
800S250x68	MS1200-10D-CCW	1.324	0.695	0.363	0.438	1.38	0.424	0.33	1.03
800S250x54	MS1200-10D-CCW	1.076	0.566	0.225	0.289	1.59	0.284	0.27	1.02
600S200x97	MS1200-10D-CCW	0.891	0.464	0.600	0.527	0.88	0.480	0.59	1.10
600S200x68	MS1200-10D-CCW	0.665	0.347	0.287	0.288	1.10	0.284	0.43	1.01
600S200x54	MS1200-10D-CCW	0.544	0.284	0.179	0.192	1.26	0.197	0.35	0.98

Table 3 continued from previous page

Section	Type	B_p kN-m^2	B_y kN-m^2	B_{crd} kN-m^2	$B_{n\sigma}$ kN-m^2	λ_B	B_{npred} kN-m^2	$\frac{B_{n\sigma}}{B_p}$	$\frac{B_{n\sigma}}{B_{npred}}$
12Z325x070	MS1200-10D-CW	4.442	2.321	0.528	0.752	2.10	0.756	0.17	1.00
12Z325x059	MS1200-10D-CW	3.730	1.950	0.361	0.511	2.32	0.533	0.14	0.96
8Z275x059	MS1200-10D-CW	1.924	1.049	0.254	0.328	2.03	0.345	0.17	0.95
6Z225x070	MS1200-10D-CW	1.274	0.678	0.275	0.330	1.57	0.341	0.26	0.97
6Z225x059	MS1200-10D-CW	1.070	0.569	0.188	0.226	1.74	0.245	0.21	0.92
1200S300x97	LargeLip-10D-CCW	1.169	0.636	1.871	0.912	0.58	0.849	0.78	1.07
1200S300x68	LargeLip-10D-CCW	0.851	0.464	0.895	0.492	0.72	0.541	0.58	0.91
1200S300x54	LargeLip-10D-CCW	0.688	0.375	0.555	0.354	0.82	0.393	0.52	0.90
1000S300x97	LargeLip-10D-CCW	0.943	0.500	1.559	0.744	0.57	0.695	0.79	1.07
1000S300x68	LargeLip-10D-CCW	0.687	0.365	0.751	0.395	0.70	0.446	0.57	0.88
1000S300x54	LargeLip-10D-CCW	0.555	0.295	0.469	0.287	0.79	0.327	0.52	0.88
800S250x97	LargeLip-10D-CCW	0.553	0.292	1.286	0.486	0.48	0.442	0.88	1.10
800S250x68	LargeLip-10D-CCW	0.405	0.214	0.622	0.259	0.59	0.293	0.64	0.88
800S250x54	LargeLip-10D-CCW	0.329	0.174	0.388	0.190	0.67	0.219	0.58	0.87
600S200x97	LargeLip-10D-CCW	0.287	0.151	0.979	0.260	0.39	0.245	0.91	1.06
600S200x68	LargeLip-10D-CCW	0.212	0.111	0.477	0.135	0.48	0.169	0.64	0.80
600S200x54	LargeLip-10D-CCW	0.173	0.091	0.299	0.098	0.55	0.129	0.57	0.76
1200S300x97	Mild2x-6D-CCW	1.950	1.045	1.113	0.963	0.97	0.955	0.49	1.01
1200S300x68	Mild2x-6D-CCW	1.427	0.769	0.523	0.514	1.21	0.542	0.36	0.95
1200S300x54	Mild2x-6D-CCW	1.155	0.624	0.321	0.352	1.39	0.366	0.30	0.96
1000S300x97	Mild2x-6D-CCW	1.575	0.824	0.919	0.792	0.95	0.790	0.50	1.00
1000S300x68	Mild2x-6D-CCW	1.153	0.606	0.433	0.426	1.18	0.452	0.37	0.94
1000S300x54	Mild2x-6D-CCW	0.934	0.492	0.268	0.301	1.35	0.308	0.32	0.98
800S250x97	Mild2x-6D-CCW	0.898	0.469	0.764	0.565	0.78	0.534	0.63	1.06
800S250x68	Mild2x-6D-CCW	0.662	0.347	0.363	0.297	0.98	0.321	0.45	0.93
800S250x54	Mild2x-6D-CCW	0.538	0.283	0.225	0.219	1.12	0.225	0.41	0.97
600S200x97	Mild2x-6D-CCW	0.446	0.232	0.600	0.348	0.62	0.312	0.78	1.12
600S200x68	Mild2x-6D-CCW	0.333	0.174	0.287	0.192	0.78	0.199	0.58	0.97
600S200x54	Mild2x-6D-CCW	0.272	0.142	0.179	0.137	0.89	0.145	0.50	0.95
8Z275x105	Mild2x-6D-CW	1.736	0.945	0.945	0.866	1.00	0.823	0.50	1.05
8Z275x070	Mild2x-6D-CW	1.146	0.624	0.375	0.452	1.29	0.402	0.39	1.12
6Z225x105	Mild2x-6D-CW	0.965	0.514	0.686	0.516	0.87	0.527	0.54	0.98

4. Prediction of bimoment strength for torsion alone

A standardized direct strength prediction equation for bimoment strength B_n incorporating plastic bimoment B_p, buckling bimoment B_{cr}, and yield bimoment B_y was adopted to fit the data described in Section 3. The equation form proposed by the second and the third authors (Glauz and Schafer, 2022) is shown in Eq. 8. The numerical coefficients a and b were iterated and determined in the regression analysis by finding the optimal fit between the simulation data and the predicted data, where R^2 was used as the fit error indicator.

$$B_n = B_p \cdot \frac{B_{cr} + aB_y}{B_{cr} + bB_y} \tag{8}$$

For cases showing controlling LB or DB, different buckling bimoment (B_{crl} or B_{crd}) was adopted in Eq. 8. Therefore, the regression analyses for cases showing different buckling behaviors were
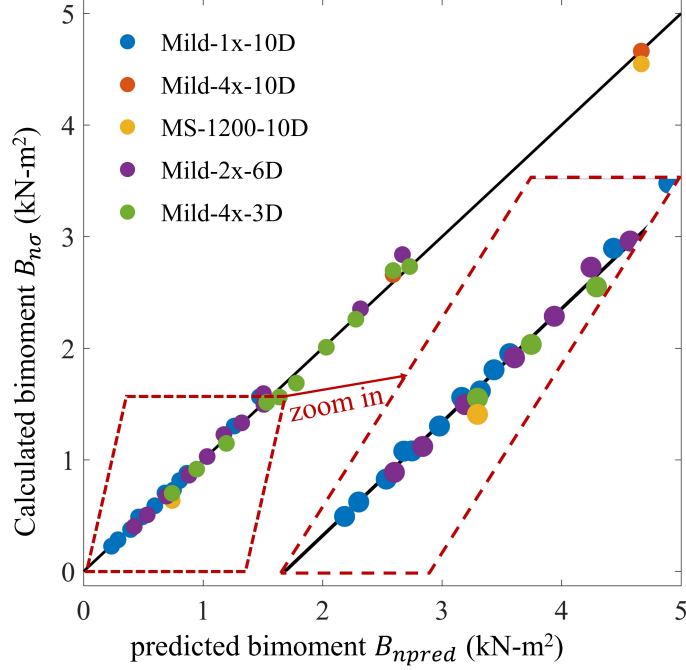
12

Figure 9: Comparison between predicted bimoment and calculated bimoment for cases showing LB behaviors

carried out respectively. For LB controlled cases, a and b were determined as 0.094 and 0.230 respectively, which led to a $R^2 = 0.997$. The comparison between the predicted bimoment strength B_{npred} and the calculated bimoment $B_{n\sigma}$ at midspan is shown in Fig. 9. The average $B_{n\sigma}/B_{npred}$ is 0.992 and the COV is 4.2%. For DB controlled cases, a and b were determined as $a = 0$ and $b = 1.110$. The R^2 for the DB controlled case is 0.979. The relationship between B_{npred} and $B_{n\sigma}$ is shown in Fig. 10. The average $B_{n\sigma}/B_{npred}$ for the DB controlled cases is 1.006, and the COV is 8.6%.

In addition, Eq. 8 can be transformed into the relationship between B_n/B_p and the slenderness for bimoment $\lambda_B = \sqrt{B_y/B_{cr}}$ as shown in Eq. 9. The curves built by Eq. 9 using the calibrated coefficients a and b for LB and DB controlled cases are shown in Fig. 11 and 12 respectively. For LB controlled cases (Fig. 11), λ_{LB} varies from 0.5 to 4 for different member geometries and steel grades, and B_n/B_p varies from 0.5 to 1. For DB controlled cases (Fig. 12), λ_{DB} various from 0.4 to 2.5, and B_n/B_p various from 0.13 to 1. For both curves, λ_B tends to increase for cases using higher strength material, and this tendency is more significant for the LB controlled cases. Additionally, B_n/B_p shows an obvious decreasing trend when λ_B increases, and the trend is more prominent for the DB controlled cases.

$$\frac{B_n}{B_p} = \frac{B_{cr} + aB_y}{B_{cr} + bB_y} = \frac{1 + a\lambda_B{}^2}{1 + b\lambda_B{}^2} \tag{9}$$

The comparisons shown in Fig. 9 to 12 indicate the adopted equation (Eq. 8) with calibrated coefficients show excellent agreement between the prediction and the whole set of simulation data from a wide range of different materials and member geometries. In other words, the chosen bimoment
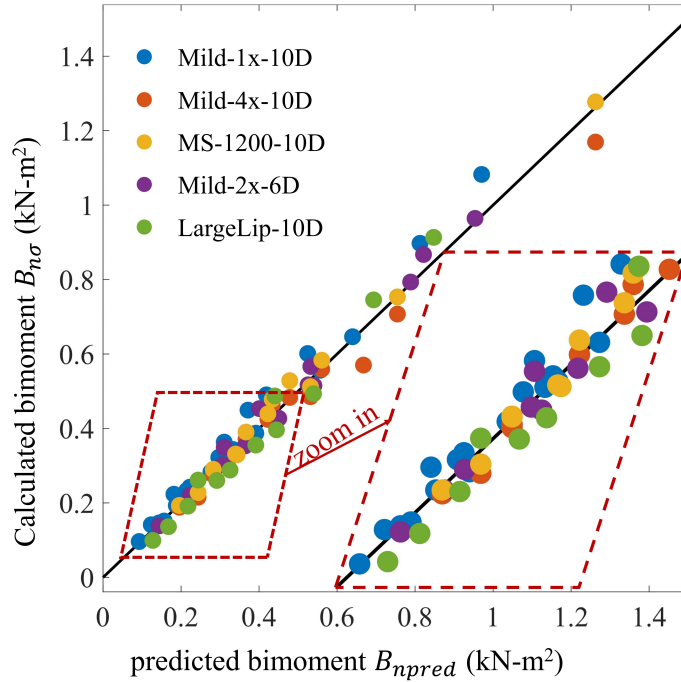
13

Figure 10: Comparison between predicted bimoment and calculated bimoment for cases showing DB behaviors
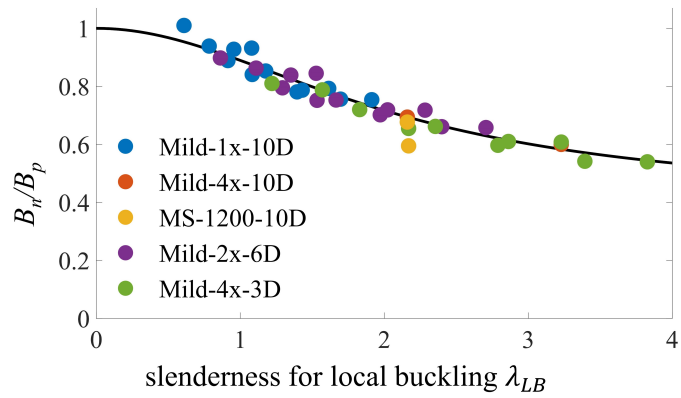

Figure 11: Proposed bimoment strength curve considering local slenderness compared with FEA simulation data
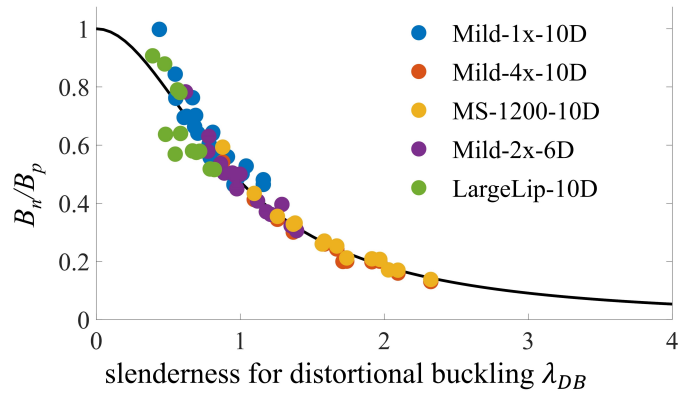

Figure 12: Proposed bimoment strength curve considering distortional slenderness compared with FEA simulation data

14

strength equation and the calibrated coefficients might work well for other CFS members.

5. Conclusions

A simple method to predict thin-walled CFS member bimoment capacity has been developed. A set of bimoment parameters, including yield bimoment B_y, plastic bimoment B_p, buckling bimoment B_{cr}, and bimoment strength B_n, are calculated and determined using a validated finite element model considering buckling and/or inelastic behaviors. A wide range of steel grades with yield strengths from conventional mild steel to ultra high-strength steel and different typical Cee and Zee sections are investigated. A simple and uniform equation is adopted to predict the bimoment strength B_n of CFS member incorporating B_y, B_p, and B_{cr}. The calibrated coefficients of the equation for local buckling and distortional buckling are proposed respectively based on the regression analyses. Excellent agreements between the adopted equation with calibrated coefficients and simulation data show the validity of the equation. Furthermore the wide range of cross section geometries and steel grades being considered indicate the equation and calibrated coefficients might be applicable to other common geometries and steel grades in the CFS market. Additional ongoing work to develop a reliable database and predict bimoment capacity of CFS open sections for cases under combined torsion and bending with various boundary conditions are in progress.

References

Abaqus (2016). *version 6.16*. Dassault Systèmes Simulia Corp.

American Iron and Steel Institute (2020). *S100-16 (R2020): North American Specification for the Design of Cold-formed Steel Structural Members*. Washington, DC, U.S.A.

American Iron and Steel Institute (AISI) (2017). *D100-17: AISI Manual Cold-Formed Steel Design*. Washington, DC, U.S.A.

Bian, Guanbo et al. (2016). "Torsion of cold-formed steel lipped channels dominated by warping response". In: *Thin-Walled Structures* 98, pp. 565–577.

European Committee for Standardization (CEN) (2006). *Eurocode 3: Design of steel structures, Part 1-3: General rules - Supplementary rules for cold-formed members and sheeting*. Brussels, Belgium, pp. 1–130.

Glauz, Robert S (2020). "Torsion Analysis for Cold-Formed Steel Members Using Flexural Analogies". In: *Proceedings of the Cold-Formed Steel Research Consortium Colloquium*. URL: `http://jhir.library.jhu.edu/handle/1774.2/63139`.

Glauz, Robert S and Benjamin W. Schafer (2022). "Modifications to the Direct Strength Method of cold-formed steel design for members unsymmetric about the axis of bending". *Submitted to Thin-Walled Structures - under review*.

Li, Zhanjie and Benjamin W. Schafer (2010). "Buckling Analysis of Cold-formed Steel Members with General Boundary Conditions Using CUFSM Conventional and Constrained Finite Strip Methods". In: *CCFSS Proceedings of International Specialty Conference on Cold-Formed Steel Structures (1971 - 2018)*. St. Louis, Missouri, U.S.A.

Ministry of Construction of the P.R.C and General Administration of Quality Supervision, Inspection and Quarantine of the P.R.C (2002). *Technical code of cold-formed thin-wall steel structures*. Beijing, China, pp. 1–93.

Steel Stud Manufacturers Association (SSMA) (2015). *SSMA Product Technical Guide*. Boise, ID, U.S.A.

Wan, Hong Xia, Bin Huang, and Mahen Mahendran (2021). "Experiments and numerical modelling of cold-formed steel beams under bending and torsion". In: *Thin-Walled Structures* 161, p. 107424. ISSN: 02638231. DOI: 10.1016/j.tws.2020.107424.

Xia, Yu et al. (2021). "Numerical modeling of stress-strain relationships for advanced high strength steels". In: *Journal of Constructional Steel Research* 182, p. 106687. ISSN: 0143974X. DOI: 10.1016/j.jcsr.2021.106687.

Zeinoddini-Meimand, Vahid (2011). "Geometric imperfections in cold-formed steel members". English. PhD thesis, p. 280. ISBN: 978-1-267-15044-8.